Electronic Supplementary Material (ESI) for Physical Chemistry Chemical Physics.

Supporting information

Imaging Aβ(1–42) fibril elongation reveals strongly polarised growth and growth incompetent states

*Laurence J Young, Gabriele S Kaminski Schierle, Clemens F Kaminski**

Supporting Figures

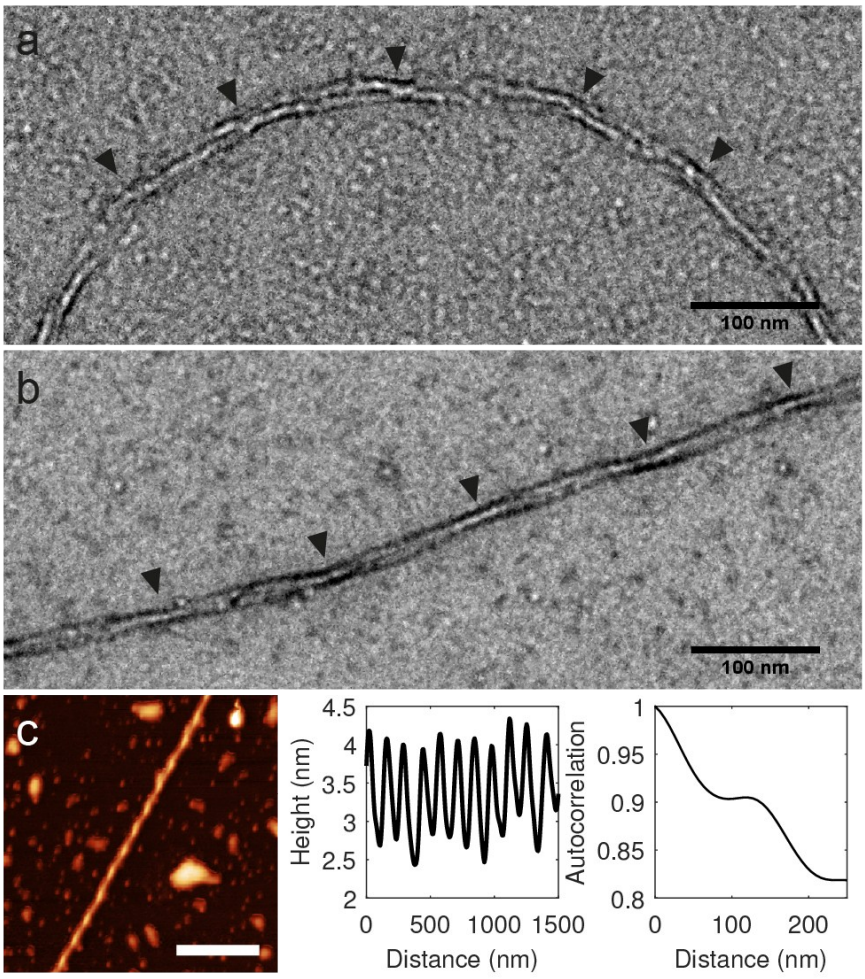

Figure S1. Fluorescent labelling does not affect fibril morphology. Negative stain transmission electron microscopy of (a) unlabelled and (b) 10% Hilyte Fluor647 labelled Aβ42 fibrils formed from initial 50 μM monomer concentration in aggregation buffer (20 mM sodium phosphate buffer, 200 μM EDTA, pH 7.4) at 37°C without agitation. Scale bars 100 nm. (c) AFM of 10% HF647 fibrils, with line profile and autocorrelation of fibril height. Scale bar 500 nm. The fibrils have a width of ~7 nm and are composed of two protofilaments. Both labelled and unlabelled

fibrils show helical periodicity with a crossover distance of 110 to 130 nm. Cross over points of of intertwining protofibrils are indicated by black triangles in panels a, and b.

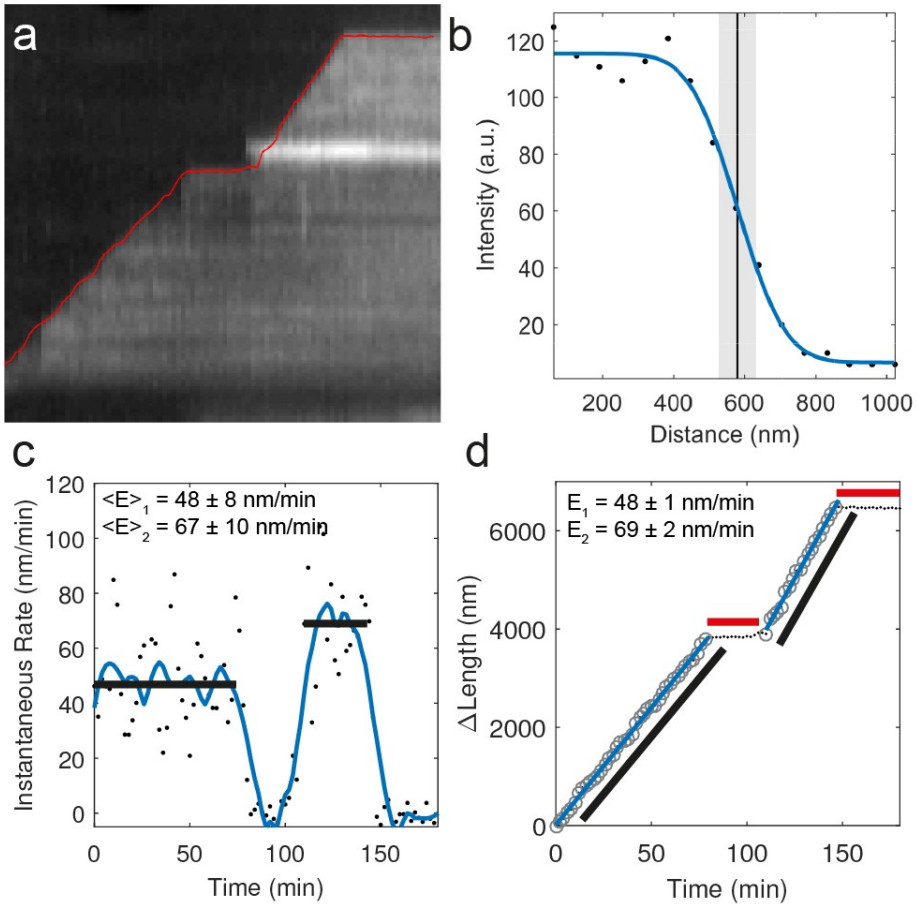

Figure S2. Image analysis method for kymograph edge fitting. (a) Each fibril is traced using a segmented line and a maximum intensity kymograph projection is produced. The growing edge of the fibril is then found by fitting a complementary error function (erfc) to the image intensity at each time point in the kymograph. (b) The fibril end position is estimated as the mean of the erfc fit. (c) Instantaneous elongation rate. The instantaneous elongation rate is calculated as the difference in fibril length between successive time points. The mean instantaneous rate for the two growth periods shown here is 48 ± 8 nm/min and 67 ± 10 nm/min (mean ± S.D.) respectively. The measurement of instantaneous elongation rate is affected by differences in the experimental signal-to-ratio. (d) Fitted elongation rate. As the fibril growth rate is constant during growing periods, a more robust method of extracting the elongation rate is to fit each growth period with a first order

polynomial. The slope of the line gives elongation rates of 48 ± 1 nm/min and 69 ± 2 nm/min (slope ± 95% confidence intervals).

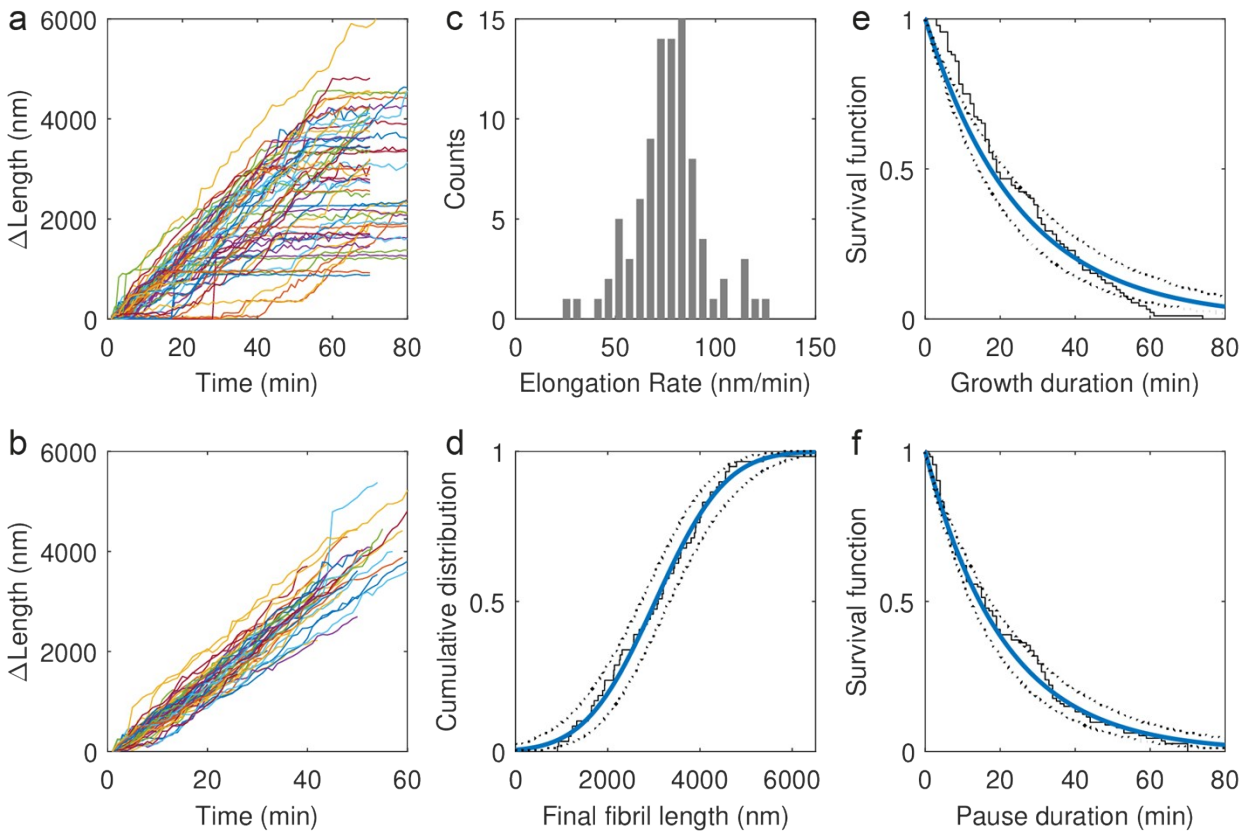

Figure S3. Analysis of multiple fibril traces showing the parameters that can be extracted from an ensemble of single fibril traces. 10 μM Aβ42 concentration, 37 °C, N = 59. (a) Fast end fibril traces obtained using method shown in Figure S2, (b) Fibril traces with paused sections removed, (c) Histogram of pause-free elongation rates obtained *via* fitting growing sections. Elongation rate 76.2 ± 17.9 nm/min (mean ± S.D.) (d) Cumulative distribution of the final fibril length with normal distribution fit (solid line) and 95% CI. (broken lines). Final length 3.03 ± 1.20 μm (mean ± S.D.) (e-f) Growth and pause duration distributions with single exponential fits (solid line) and 95% CI (broken lines). Growth duration 25.1 ± 10.5 min, pause duration 21.0 ± 7.9 min (mean ± 95% CI).

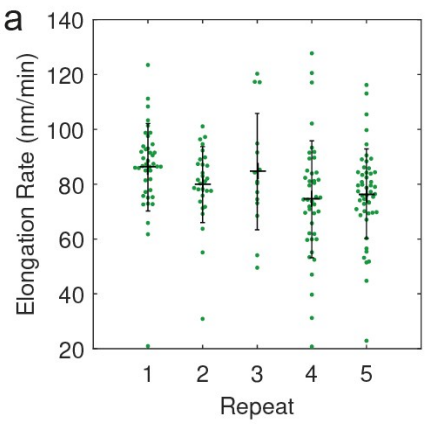

Repeat	Duration (min)	Fibrils	Growing sections	Mean rate ± std (nm/min)
1	60	32	41	86.2 ± 5.03
2	60	21	29	79.8 ± 5.27
3	27	10	15	84.6 ± 11.8
4	90	28	43	74.5 ± 6.64
5	70	32	50	76.5 ± 4.63

Figure S4. Reproducibility of elongation rate measurements of fibril fast growing ends. Repeats 1, 2 and 3 were performed on different days with different monomer preparations (10 µM monomer, 5% labelled, 37 °C). Repeats 4 and 5 were performed on the same day with the same monomer preparation. One-way ANOVA yields a small but significant difference between repeats performed on different days with different monomer preparation, $P(F > 2.98) = 0.02$. For the repeats 4 and 5 using the same monomer preparation, a two-sample t-test yields no significant difference ($p = 0.603$). We therefore used the same starting monomer preparation when performing concentration and temperature dependent measurements.

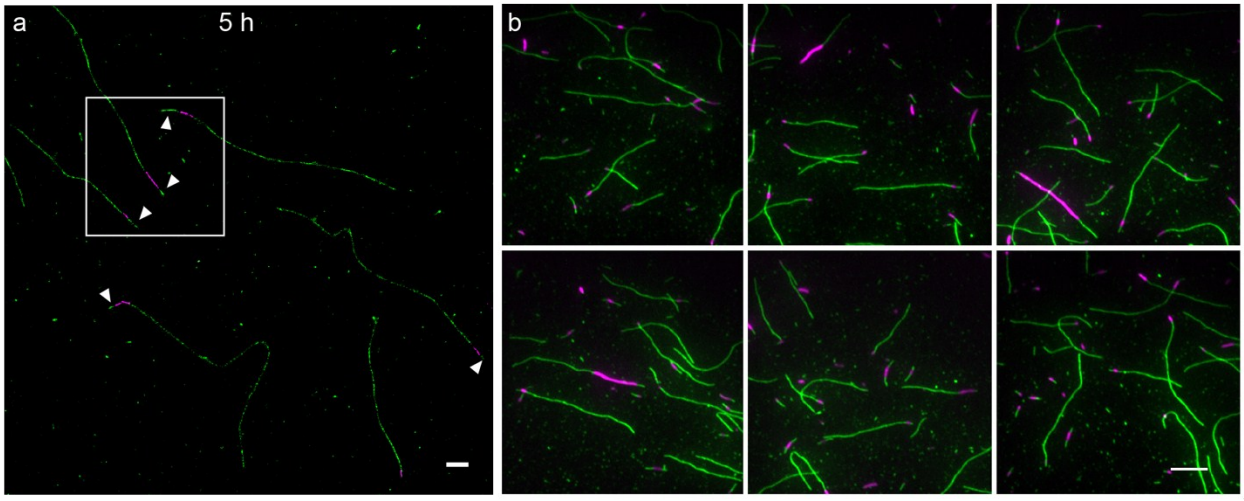

Figure S5. Examples of two colour fibrils imaged *ex situ* after 5 h. (a) Full *d*STORM image of inset presented in Figure 4b. Arrows denote slow end growth. Scale bar 1 µm. (b) Standard TIRF microscopy. Histograms in Figure 4 were produced by manual tracing of slow and fast ends from 85 separate regions of interest and 469 fibrils. Scale bar 5 µm.

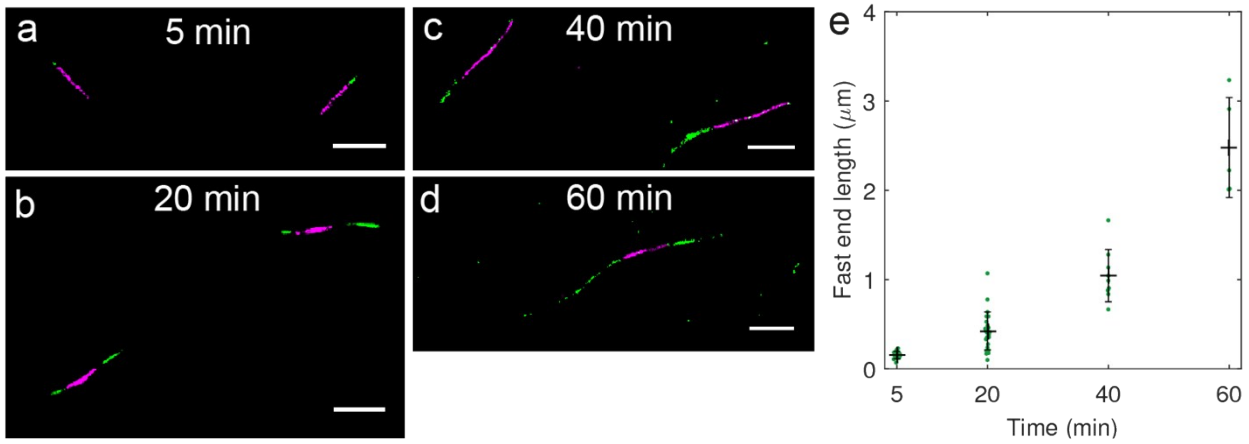

Figure S6. *d*STORM imaging the time course of elongation *ex situ*. 10 μM Aβ42 monomer concentration. HF647-labelled seed fibrils (magenta) were incubated with 10 μM monomeric Aβ42 (5% labelled) in low binding tubes, and incubated in a heating block at 37 °C. Samples were removed at successive time points after addition of monomer (5, 20, 40, 60 minutes) and dropped onto coverslips (ibidi). The elongation reaction was quenched *via* addition of an excess of buffer prior to two colour *d*STORM imaging. (a) After 5 minutes incubation, attachment of monomer is primarily at one end of the seed. (b-d) After further incubation, fibrils begin to show bipolar growth. Scale bars 1 μm. (e) Measurement of the fast end lengths at each time point results in an apparent elongation rate of 40 nm/min.

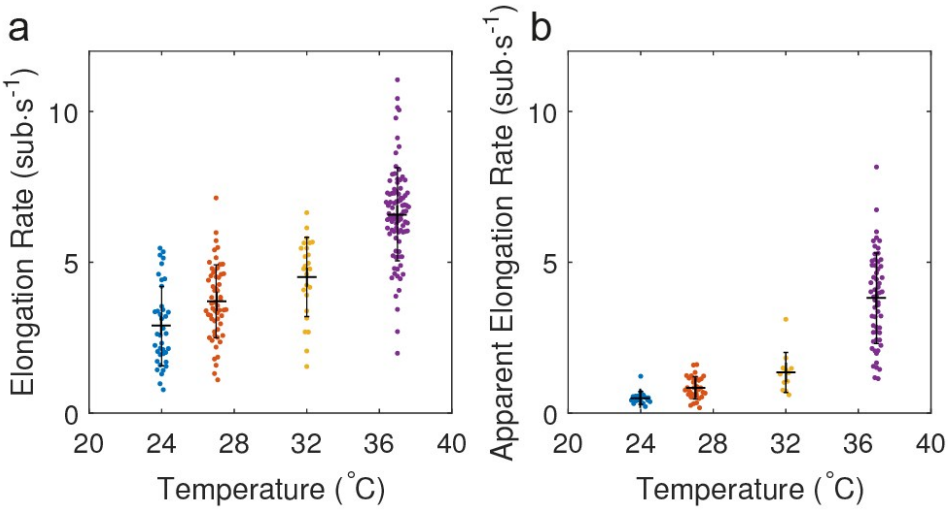

Figure S7. Underestimation of the elongation rate from fibril length measurements. (a) Pause-free elongation rates obtained from fitting only the growing sections, (b) Apparent elongation rates

calculated from the final fibril lengths measured at the end of each elongation assay. Previous bulk measurements of the energy of activation for elongation were likely a convolution of two energy barriers: the barrier for monomer addition onto the end of a growth competent fibril (growing), and the barrier for transition between the paused and growing state. As the pause duration is observed to decrease with temperature this would increase the slope of the Arrhenius plot, giving a higher value for the energy barrier.

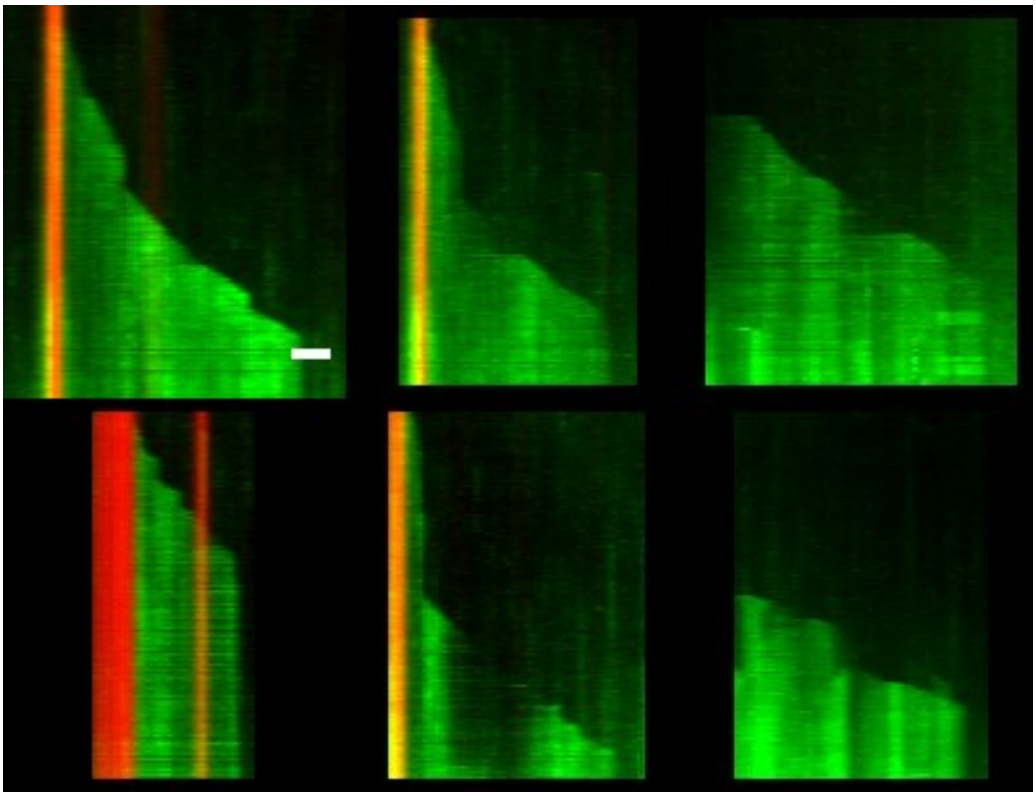

Figure S8. Kymographs for Aβ42 elongation produced using recombinant protein (gift of Prof Sara Linse, see Supporting Methods for details). Monomeric stock solutions were produced using protocols as described in Silvers et al.[1]. Protocol for elongation as described above for the synthetic variants. Clearly stop and go events are also observed, as well as asymmetric end growth.

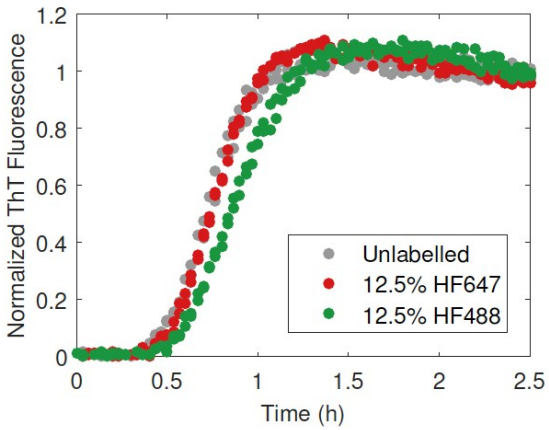

Figure S9. The nucleation and growth kinetics of Aβ42 peptides are not significantly affected by the presence of HF488 and HF647 dyes at the labelling ratios used in the present experiments. The graph shows nucleation and growth using a ThT assay of monomeric and labelled Aβ42 in comparison with unlabelled control. Up to labelling ratios of 10% there was no evidence for any changes in the kinetics of the reaction. At a ratio of up to 12.5% labelled to unlabelled monomers slight deviations begin to emerge for the HF488 labelled sample, as seen in the figure. The experiments were performed using stock solutions containing monomers of labelled and unlabelled Aβ42, and unlabelled controls. Samples were gel filtrated using SEC-FPLC to ensure monomeric starting conditions (see Supporting Methods). Clearly there is hardly any effect on lag phase and growth kinetics. In separate experiments (data not shown) we estimated the dye loading onto the elongating fibrils from the dye fluorescence intensities and from this found no evidence that the likelihood of monomer addition to the fibril ends differs for labelled or unlabelled monomers at the stated labelling ratios.

Supporting Video 1. Apparent unipolar Aβ42 fibril growth (stills shown in Figure 1b).

Supporting Video 2. *in situ* TIRF microscopy of Aβ42 fibril elongation from preformed seeds (stills shown in Figure 1c).

Supporting Methods

Image analysis

Correction of lateral drift was performed after acquisition using the Descriptor Based Registration plugin in ImageJ[2], and the chromatic offset between the 640 and 488 nm channel corrected using a 2D translation, with co-ordinates determined from positions of multicolour fluorescent beads. New growth onto the ends of existing fibril seeds was analysed *via* kymograph projections (Supplementary Fig. 2). Each fibril was traced manually using segmented line sections (10 pixels wide) in ImageJ and a maximum intensity kymograph projection was produced. As the elongating fibrils did not dissociate or bend appreciably from frame to frame, data analysis was simplified as a kymograph can be generated by projecting the fibril intensity over time with a single segmented line, rather than by tracing the length of the fibril manually in every frame. Kymographs were analysed using custom MATLAB code to extract the position of the fibril end by fitting the end intensity to a complementary error function[3]. Each growth period of the fibril end trace was selected manually and fitted with a one dimensional polynomial function *via* linear regression. The slope of the fit was used to calculate the elongation rate for each growth period. More than 15 fibril traces were analysed per condition with most fibrils exhibiting more than one growth period over the duration of the assay. Each data point in the plots in Figure 2 represents the fitted rate of a single growth period.

Transmission electron microscopy

Amyloid fibril samples were adsorbed on glow-discharged, carbon-coated grids and negatively stained with 2% uranyl acetate. Grids were viewed using a FEI Tecnai G2 electron microscope operating at 200 keV (Cambridge Advanced Imaging Centre).

Atomic force microscopy (AFM)

Amyloid fibril samples were adsorbed onto freshly cleaved mica substrates, rinsed with ddH2O and imaged in air using a Veeco Dimension 3100 AFM (Bruker, Cambridge, UK) in tapping mode. Silicon cantilevers with a resonant frequency of 310 kHz and tip radius of 10 nm (MicroMasch) were used.

Thermodynamic model for determination of free energy and entropy

In principal, the activation energy E_a obtained from the slope of the Arrhenius plot of log(r) against inverse temperature must be corrected to account for both the difference between internal energy and enthalpy, and the temperature dependence of the frequency factor (i.e. the kinetic prefactor) as described by Buell et al[4]. However, as both are negligible over the experimental temperature range, $\Delta H^{\ddagger}$ can be equated to the activation energy obtained from the slope of the Arrhenius plot.

In order to calculate the activation free energy $\Delta G^{\ddagger}$ we approximate the diffusive prefactor using a combination of polymer theory with Kramer's problem of escape from a metastable state. In this model, the addition of a monomeric protein onto the end of an amyloid fibril can be described simply by the total flux of monomers moving over a single energy barrier[5]:

$$\Phi = \frac{Dcr_{eff}}{1 + Dcr_{eff}\tau_R} e^{-\frac{G^{\ddagger}}{RT}}$$

For low concentrations of monomeric peptide below the saturation regime, this expression yields the limit $\Phi = \phi_{max} e^{-\frac{G^{\ddagger}}{RT}}$ where $\phi_{max} = Dcr_{eff}$ is maximal barrierless flux, or the diffusion limited elongation rate. This maximum rate depends on the diffusion coefficient of the monomer *D*, its concentration *c*, and a characteristic distance r_{eff} which defines the effective reaction volume at the end of the fibrils. Measurements of the diffusion coefficient of unlabelled Aβ(1-40) using PFG-NMR have yielded values of $1.3 - 1.5 \times 10^{10}$ m^2s^{-1} [6,7], while fluorescence correlation spectroscopy (FCS) measurements yielded values of $1.33 - 1.45 \times 10^{10}$ m^2s^{-1} for HiLyte Fluor 647 labelled Aβ(1-42)[8]. These studies suggest that there is a negligible difference between the diffusion coefficient of labelled and unlabelled Aβ. As these measurements were performed at 25 ºC, here we adjust for the temperature dependence of the diffusion coefficient by $\frac{D_{T1}}{D_{T1}} = \frac{\mu_2 T_1}{\mu_1 T_2}$, where μ is the dynamic viscosity of water, resulting in a diffusion coefficient at 37 ºC of 2.0×10^{10} m^2s^{-1}. The characteristic distance r_{eff} (0.347 Å) is computed from $r_{eff} = \frac{b_0}{\pi\sqrt{2n}}$ where b_0 is the Kuhn length (1 nm) and *n* is the length of the peptide (n = 42 amino acids). This inverse relationship between reaction volume and protein size arises because the theory explicitly takes into account not only

translational diffusion of the whole protein into a volume close to the fibril end, which would scale linearly with the size of the protein, but also diffusion of internal degrees of freedom, arising from the movement of protein segments relative to each other[1]. This decreasing probability with increasing protein size can be expressed as a decreasing effective reaction volume. The maximal barrierless flux, ϕ_{max}, at 10 μM Aβ42 concentration and 37 ºC is therefore 68.8 subunits/s, corresponding to a diffusion limited elongation rate of 800 nm/min.

Having estimated the kinetic prefactor, the activation free energy for elongation can then be calculated from:

$$\Delta G^{\ddagger} = RT\log\left(\frac{\phi_{obs}}{\phi_{max}}\right)$$

where ϕ_{obs} is equivalent to the absolute elongation rate $r = 2.44E/0.47$ that we can extract from measurements of individual fibrils. The histogram of activation free energies presented in the inset of Figure 2E is calculated from individual fibril rates from assays with a monomer concentration in the linear regime (ie. for 2.5 and 5 μM). We take into account the concentration dependent diffusion limited rate, ϕ_{max}, which is 8.6 and 17.2 subunits/s, or 99.4 and 199.0 nm/min, for 2.5 and 5 μM respectively.

Super-resolution microscopy (*d*STORM)

Two-colour super-resolution microscopy was performed as previously described using an inverted total internal reflectance fluorescence (TIRF) microscope[9,10]. HiLyte Fluor 647 and 488 dyes were excited with a 640 nm diode laser (Toptica) and 490 nm laser (Cobolt) respectively with an irradiance between 1-5 kW/cm². Fluorescence was collected using a 100X/1.49 NA objective (Nikon) onto an EMCCD camera (iXon3 897, Andor). To induce dye photoswitching the samples were immersed in a switching buffer consisting of 100 mM mercaptoethylamine (Sigma) in PBS at pH 8.2 supplemented with an oxygen scavenger to reduce photobleaching (40 mg/ml glucose, 50 μg/ml glucose oxidase, 1 μg/ml catalase). The 640 nm and 488 nm channels were imaged sequentially *via* band-pass filters (676/37 and 520/40, Semrock), and a series of 15,000 frames was acquired with 15 ms exposure time for each field of view. All image stacks were analysed using rapidSTORM 3.3[11] and super-resolution images were produced with a pixel size of 20 nm.

[1] Private communication with Dr A.K. Büll.

Recombinant protein labelling

Unlabelled recombinant Aβ(M1-42) was a gift from Prof Sara Linse and was produced using protocols as described in Silvers et al.[1]. Labelled recombinant protein was produced by maleimide labelling of an N-terminal cysteine variant, Aβ(MC1-42). Aβ(MC1-42) was purified in the same manner as for Aβ(MC1-42) but with 1mM DTT in the purification buffer to prevent disulphide bond formation. The purified peptide was aliquoted and lyophilized. Multiple lyophilized aliquots were pooled and dissolved in 6 M GuHCl with 1 mM DTT, then run through SEC-FPLC (Superdex® 75 10/300 GL, Sigma) on a fast protein liquid chromatography (FPLC) system (ÄKTAxpress, GE Healthcare) equilibrated with 20 mM sodium phosphate buffer to isolate the monomer and remove DTT. The monomer fraction was collected on ice and peptide concentration was determined from the average absorbance at 280 nm. HiLyte™ Fluor 488 (HF488) C2 maleimide (Anaspec, USA) was dissolved in anhydrous DMSO, and 3 molar equivalents of the dye were added to the Aβ(MC1-42) followed by gentle mixing. The reaction was left to proceed overnight at 4 °C. Labelled HF488-Aβ(MC1-42) was isolated from the free dye and aggregates again by SEC-FPLC using 20 mM sodium phosphate + 200 μM EDTA as the elution buffer. The labelled peptide was collected on ice, followed by lyophilization and storage at -80 °C. Labelled peptide concentration was determined from the absorbance at 497 nm. For the recombinant elongation assay shown in Figure S8, lyophilized peptide aliquots were dissolved in 20mM NaP + 200 M EDTA and used without further purification.

References

(1) Silvers, R.; Colvin, M. T.; Frederick, K. K.; Jacavone, A. C.; Lindquist, S. L.; Linse, S.; Griffin, R. G. *Biochemistry* **2017**, acs. biochem.7b00729.

(2) Preibisch, S.; Saalfeld, S.; Schindelin, J.; Tomancak, P. *Nat. Methods* **2010**, *7* (6), 418.

(3) Demchouk, A. O.; Gardner, M. K.; Odde, D. J. *Cell. Mol. Bioeng.* **2011**, *4* (2), 192.

(4) Buell, A. K.; Dhulesia, A.; White, D. A.; Knowles, T. P. J.; Dobson, C. M.; Welland, M. E. *Angew. Chemie Int. Ed.* **2012**, *51* (21), 5247.

(5) Buell, A. K.; Blundell, J. R.; Dobson, C. M.; Welland, M. E.; Terentjev, E. M.; Knowles, T. P. J. *Phys. Rev. Lett.* **2010**, *104* (22), 228101.

(6) Tseng, B. P.; Esler, W. P.; Clish, C. B.; Stimson, E. R.; Ghilardi, J. R.; Vinters, H. V; Mantyh, P. W.; Lee, J. P.; Maggio, J. E. *Biochemistry* **1999**, *38*, 10424.

(7) Danielsson, J.; Jarvet, J.; Damberg, P.; Gräslund, A. *Biochemistry* **2004**, *43* (20), 6261.

(8) Wennmalm, S.; Chmyrov, V.; Widengren, J.; Tjernberg, L. *Anal. Chem.* **2015**, *87* (23), 11700.

(9) Pinotsi, D.; Buell, A. K.; Galvagnion, C.; Dobson, C. M.; Kaminski Schierle, G. S.; Kaminski, C. F. *Nano Lett.* **2014**, *14* (1), 339.

(10) Pinotsi, D.; Michel, C. H.; Buell, A. K.; Laine, R. F.; Mahou, P.; Dobson, C. M.; Kaminski, C. F.; Kaminski Schierle, G. S. *Proc. Natl. Acad. Sci. U. S. A.* **2016**.

(11) Wolter, S.; Löschberger, A.; Holm, T.; Aufmkolk, S.; Dabauvalle, M.-C.; van de Linde, S.; Sauer, M. *Nat. Methods* **2012**, *9* (11), 1040.